

Locating the QCD critical point from first principles through contours of constant entropy density

Hitansh Shah,¹ Mauricio Hippert,² Jorge Noronha,³ Claudia Ratti,¹ and Volodymyr Vovchenko¹

¹*Department of Physics, University of Houston, Houston, TX 77204, USA*

²*Instituto de Física, Universidade do Estado do Rio de Janeiro,*

Rua São Francisco Xavier, 524, Rio de Janeiro, RJ, 20550-013, Brazil

³*Illinois Center for Advanced Studies of the Universe & Department of Physics,*

University of Illinois at Urbana-Champaign, Urbana, IL 61801-3003, USA

(Dated: October 22, 2024)

We propose a new method to investigate the existence and location of the conjectured high-temperature critical point of strongly interacting matter via contours of constant entropy density. By approximating these lines as a power series in the baryon chemical potential μ_B , one can extrapolate them from first-principle results at zero net-baryon density, and use them to locate the QCD critical point, including the associated first-order and spinodal lines. As a proof of principle, we employ currently available continuum-extrapolated first-principle results from the Wuppertal–Budapest collaboration to find a critical point at a temperature and a baryon chemical potential of $T_c = 114.3 \pm 6.9$ MeV and $\mu_{B,c} = 602.1 \pm 62.1$ MeV, respectively. We advocate for a more precise determination of the required expansion coefficients via lattice QCD simulations as a means of pinpointing the location of the critical endpoint in the phase diagram of strongly interacting matter.

Introduction. One of the most challenging questions in the field of quantum chromodynamics (QCD) concerns the existence of a first-order phase transition at finite baryon chemical potential μ_B and high temperature T , separating the hadronic and quark-gluon plasma phases. From state of the art lattice QCD calculations, we know that the transition from hadronic matter to deconfined quark gluon plasma at $\mu_B = 0$ is an analytic, smooth crossover [1], taking place at a pseudocritical temperature of 155 – 158 MeV [2, 3]. Because direct lattice QCD simulations are not feasible at finite density due to the fermion sign problem, whether a first-order phase transition occurs at large chemical potential remains an open question. Extrapolations of lattice results to small baryon densities indicate that the analytic crossover persists at least up to $\mu_B/T \lesssim 3$ [2, 4, 5], although a hint of a narrowing of the crossover towards large μ_B was observed for the first time in [6]. Several effective QCD theories predict a first-order phase transition at large μ_B , originating from a critical point (CP) where the transition is of second order (for recent reviews, see [7, 8]). While in the past the theoretical predictions for the location of the QCD critical point were scattered all over the QCD phase diagram, more recent ones seem to concentrate around a considerably narrower region, with chemical potentials in the range $400 \leq \mu_B \leq 650$ MeV [9–14].

The universal features and peculiar behavior expected near the QCD critical point make a compelling case for its experimental search in heavy-ion collisions, in particular utilizing event-by-event fluctuations in multiplicities of produced particles [15–17]. The experimental search for the QCD critical point is one of the primary goals of the Beam Energy Scan program at RHIC, which finished its runs in 2021 [7, 18]. Proton cumulants are expected to show characteristic signatures of critical behavior, although interpreting experimental results in this context is quite challenging. The data from the STAR Collabora-

tion [19, 20], including the new preliminary data from BESII on proton number factorial cumulants [21], hint at an interesting behavior for energies $\sqrt{s_{NN}} \leq 20$ GeV. These features cannot be explained by non-critical baselines [22, 23], even though no conclusive statement on the critical point existence/location has been made so far either using the proton cumulants, or other considerations such as finite-size scaling [24–26].

A common strategy to sidestep the obstacles for a direct lattice QCD determination of the equation of state at high baryon densities is to rely on extrapolations from zero or imaginary chemical potentials, such as analytic continuation and Taylor expansion [27–31]. These methods, however, tend to break down at large densities, in particular the naive Taylor expansion of the thermodynamic pressure in powers of μ_B/T is limited by non-analyticities in the complex plane, including the CP itself [32], and cannot therefore reach the CP. Recent approaches to extract information about the CP from lattice QCD results analyze the expected Lee-Yang edge singularities at complex baryon chemical potential and extrapolate down in temperature to locate the CP through their crossing of the real μ_B axis [13, 14].

In this Letter, we present a new method to locate the CP in the QCD phase diagram by utilizing the fact that the entropy density s is a multi-valued function in the region of a first-order phase transition, meaning that the existence of a CP implies crossings of constant entropy density contours. To utilize lattice QCD input, we extrapolate the entropy density contours from $\mu_B = 0$ by approximating them with an expansion in powers of μ_B . This expansion explicitly permits the crossings of these contours and does not break down due to the presence of the CP. Thus, the method allows for the determination of whether and where a CP is found in the phase diagram, as well as yielding spinodal and coexistence lines for the QCD phase transition.

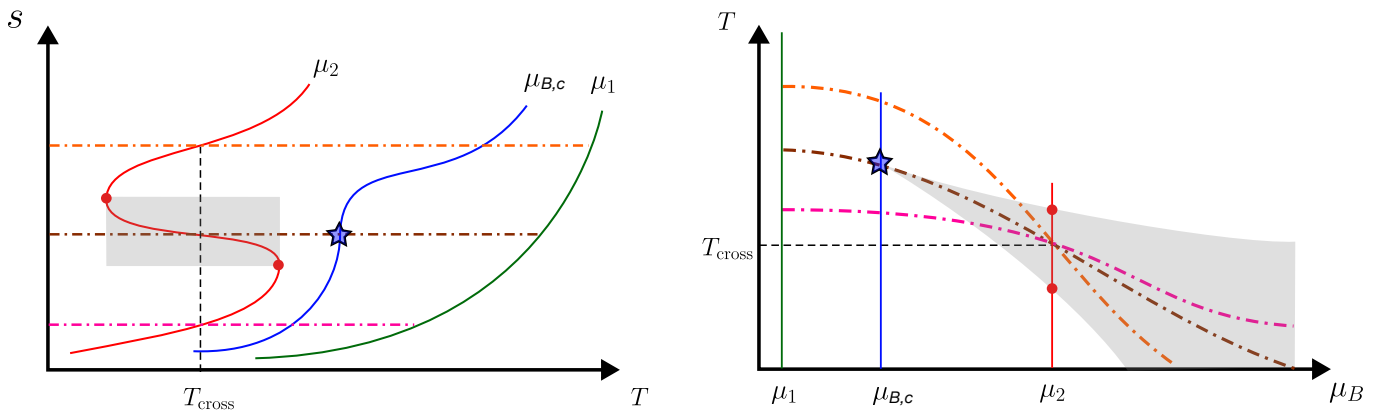


FIG. 1: Left: entropy as a function of the temperature, at three different chemical potentials. In this scheme, $\mu_1 < \mu_{B,c} < \mu_2$. Right: corresponding constant-entropy contours in the (T, μ_B) plane. The blue star indicates the critical point, while the shaded area corresponds to the spinodal region. The red dots indicate the spinodal points for $\mu_B = \mu_2$.

To utilize the first-principles input, we extract expansion coefficients for the lines of constant entropy density from state-of-the-art lattice QCD results from the Wuppertal–Budapest collaboration. Our reconstructed entropy density agrees with the lattice QCD results from [33] up to $\mu_B/T \leq 3.5$, while developing the distinctive S-shape behavior expected from a first-order phase transition at larger chemical potentials, indicating the presence of a CP. The results do not change appreciably if we utilize the lattice QCD input for the entropy density from the HotQCD Collaboration [34]. As a consistency check, we find that the method successfully locates the known CP in the holographic model developed in [35]. Our method also shows indications for a CP at imaginary μ_B close to where the endpoint of the Roberge-Weiss transition is expected.

Crossings of entropy contours. The intuitive picture behind our approach is grounded in the multi-valued behavior of the entropy density s around a first-order phase transition. Namely the fact that, unless a Maxwell construction is employed, s can have multiple values at the same values of temperature and chemical potential — typically 3 of them — corresponding to the stable and metastable phases, as well as the (unstable) spinodal region.

The expected relationship between the temperature and entropy density in the presence of the QCD CP at finite μ_B is illustrated in Fig. 1. The curves on the left panel show s versus T for different values of the chemical potential: the critical value $\mu_{B,c}$, $\mu_1 < \mu_{B,c}$ and $\mu_2 > \mu_{B,c}$. For $\mu_B < \mu_{B,c}$, the entropy is a continuous function of the temperature, with a steep rise around the crossover region. As μ_B increases, this steep rise becomes more pronounced, making the lines of constant entropy density closer in temperature, until a diverging slope is achieved at the critical point. For $\mu_B > \mu_{B,c}$, the entropy can have three values for the same (T, μ_B) pair. Thus, up to three lines of constant s can cross at the same point in the (T, μ_B) plane. This is shown by the horizon-

tal dash-dotted lines depicting three different contours of entropy density. These contours are shown in the T - μ_B plane in the right panel of Fig. 1, where they cross at the same point. In fact, crossings between contours of constant s will spread through the region in the (T, μ_B) plane between the spinodal curves.

Precisely at the spinodal points, the temperature as a function of s displays a local maximum or minimum (see Fig. 1), so that $(\partial T/\partial s)_{\mu_B} = 0$. As the critical point is approached, the local maximum and minimum coalesce, leading to an inflection point with $(\partial^2 T/\partial s^2)_{\mu_B} = 0$, while still satisfying $(\partial T/\partial s)_{\mu_B} = 0$. The location of the CP is thus determined by a pair of equations

$$(\partial T/\partial s)_{\mu_B} = 0, \quad (\partial^2 T/\partial s^2)_{\mu_B} = 0. \quad (1)$$

Similar arguments hold for other quantities that become multivalued around the first-order phase transition and may serve as order parameters. For instance, the CP of a liquid-gas transition corresponds to the vanishing first and second derivatives of the pressure with respect to the density at constant temperature.

New expansion. We describe the contours of constant entropy density in terms of the function $T_s(\mu_B; T_0)$, defined such that

$$s[T_s(\mu_B; T_0), \mu_B] = s(T_0, \mu_B = 0). \quad (2)$$

That is, for increasing values of μ_B , one can keep the entropy fixed at $s_0 = s(T_0, \mu_B = 0)$ by choosing the temperature $T = T_s(\mu_B; T_0)$. Anchoring the entropy density contour at $\mu_B = 0$ will allow us to utilize the lattice QCD input. The expansion of $T_s(\mu_B; T_0)$ in powers of μ_B reads

$$T_s(\mu_B; T_0) \approx T_0 + \sum_{n=1}^N \alpha_{2n}(T_0) \frac{\mu_B^{2n}}{(2n)!} + \mathcal{O}(\mu_B^{2(N+1)}), \quad (3)$$

where we truncate the series at order $\mathcal{O}(\mu_B^{2N})$. Of course, $T_s(\mu_B = 0; T_0) = T_0$ by definition. Note that the expansion (3) explicitly permits the existence of the crossings

even at leading order ($N = 1$), namely $T_s(\mu_B; T_{0,1}) = T_s(\mu_B; T_{0,2})$ is possible for two different values of T_0 .

From the function $T_s(\mu_B; T_0)$, we can evaluate the conditions for the presence of a critical point and the shape of spinodal lines, following the discussion above. At the spinodal lines,

$$\left(\frac{\partial T_s}{\partial s}\right)_{\mu_B} = 0 \quad \Rightarrow \quad \left(\frac{\partial T_s}{\partial T_0}\right)_{\mu_B} = 0, \quad (4)$$

where the second equation follows from the first one due to the chain rule. At the critical point, Eq. (4) is complemented by the condition

$$\left(\frac{\partial^2 T_s}{\partial s^2}\right)_{\mu_B} = 0 \quad \Rightarrow \quad \left(\frac{\partial^2 T_s}{\partial T_0^2}\right)_{\mu_B} = 0. \quad (5)$$

Expansion coefficient α_2 . The expansion coefficients α_{2n} are evaluated at $\mu_B = 0$ and can be expressed in terms of other thermodynamic quantities (see the Supplemental Material for technical details). The expression for α_2 reads

$$\alpha_2(T_0) = -\frac{2T_0\chi_2^B(T_0) + T_0^2\chi_2^{B'}(T_0)}{s'(T_0)}. \quad (6)$$

Here $\chi_2^B = \left[\frac{\partial^2(p/T)^4}{\partial(\mu_B/T)^2}\right]_T$ is the baryon number susceptibility, $s(T_0)$ is the entropy density, and $'$ indicates the temperature derivative at a constant μ_B . High-order coefficients α_{2n} involve high-order baryon number susceptibilities and high-order temperature derivatives. We restrict the present analysis to α_2 and leave the inclusion of higher order terms for the future when more precise lattice results become available.

Lattice QCD input. As follows from Eq. (6), the input quantities consist of the temperature dependencies of the entropy density $s(T)$ and baryon number susceptibility $\chi_2^B(T)$ at $\mu_B = 0$. Continuum extrapolated results from the Wuppertal-Budapest collaboration have been presented in Ref. [36] for the former and in Ref. [33] for the latter. As our analysis relies on temperature derivatives of these two quantities, we parametrize the lattice input by the following expressions

$$\frac{s(T)}{T^3} = a \cdot \tanh\left(\frac{T - T_0}{d}\right) + b, \quad (7a)$$

$$\chi_2^B(T) = d_0 \left(\frac{2 \cdot m_p}{\pi \cdot x}\right)^{\frac{3}{2}} \cdot \frac{\exp\left(-\frac{m_p}{x}\right)}{1 + \left(\frac{x}{d_1}\right)^{d_2}} + d_3 \cdot \frac{\exp\left(-\frac{d_5^4}{x^4}\right)}{1 + \left(\frac{x}{d_1}\right)^{-d_2}}. \quad (7b)$$

Here $x = T/(200 \text{ MeV})$ and $m_p = (938/200) \approx 4.7$ is the proton mass in units of 200 MeV, as in Ref. [37]. We extract the values of the parameters and their full covariance matrix from the lattice results, taking into account strong correlations of lattice data errors between

data points of neighboring temperatures. We use the extracted covariance matrix to perform Monte Carlo sampling of the parameters to perform error analysis. This procedure and its results are described in the Supplemental Material, demonstrating that the extracted covariance matrix accurately reflects lattice QCD uncertainties. In addition, we also used smoothing splines to describe $s(T)$ and $\chi_2^B(T)$ and their temperature derivatives, as a more agnostic approach to employing the lattice input. The obtained results are consistent within errors to those obtained using the parametrization (7).

Entropy density at finite baryochemical potential. The left panel of Fig. 2 depicts the temperature dependence of the scaled entropy density s/T^3 at different values of μ_B/T : 1 (red), 1.5 (orange), 2 (purple), 2.5 (black), 3 (brown), and 3.5 (blue). The results are obtained within the new expansion described above at order $\mathcal{O}(\mu_B^2)$. As an important cross-check, we compare our results with state-of-the-art lattice QCD data from Ref. [33]. One can see excellent agreement of our results with lattice QCD. In addition, the hazy lines show the different Monte Carlo samples of our parametrization, reflecting the propagation of the errors from the lattice QCD input. The resulting spread shows good agreement with the error bars of the lattice data of Ref. [33].

The right panel of Fig. 2 shows the behavior of s/T^3 at larger chemical potentials, $\mu_B = 450 \text{ MeV}$ (red), 602 MeV (blue), and 750 MeV (orange). One can see the development of a distinct S-shaped, multi-valued behavior of the entropy density as μ_B is increased to $\mu_B \gtrsim 600 \text{ MeV}$ – a hallmark feature of a first-order phase transition.

Critical point location. The CP is determined by a pair of equations $\left(\frac{\partial T_s}{\partial T_0}\right)_{\mu_B} = 0$ and $\left(\frac{\partial^2 T_s}{\partial T_0^2}\right)_{\mu_B} = 0$. At order $\mathcal{O}(\alpha_2)$, the function $T_s(\mu_B; T_0)$ reads

$$T_s(\mu_B; T_0) = T_0 + \alpha_2(T_0) \frac{\mu_B^2}{2}. \quad (8)$$

Denoting $\mu_{B,c}$ and $T_{0,c}$ as the values of μ_B and T_0 corresponding to the CP, the first equation, $\left(\frac{\partial T_s}{\partial T_0}\right)_{\mu_B} = 0$, yields the relationship between $\mu_{B,c}$ and $T_{0,c}$:

$$1 + \alpha_2'(T_{0,c}) \frac{\mu_{B,c}^2}{2} = 0 \quad \Rightarrow \quad \mu_{B,c} = \sqrt{-\frac{2}{\alpha_2'(T_{0,c})}}. \quad (9)$$

This equation also determines the spinodal lines at $\mu_B > \mu_{B,c}$ where it has two solutions with respect to T_0 .

The second equation, $\left(\frac{\partial^2 T_s}{\partial T_0^2}\right)_{\mu_B} = 0$, corresponds to

$$\alpha_2''(T_{0,c}) = 0, \quad (10)$$

which determines $T_{0,c}$. The determination of the CP location thus proceeds by solving Eq. (10) for $T_{0,c}$, plugging the result into Eq. (9) to determine $\mu_{B,c}$, and computing $T_c = T_s(\mu_{B,c}; T_{0,c})$ through Eq. (8).

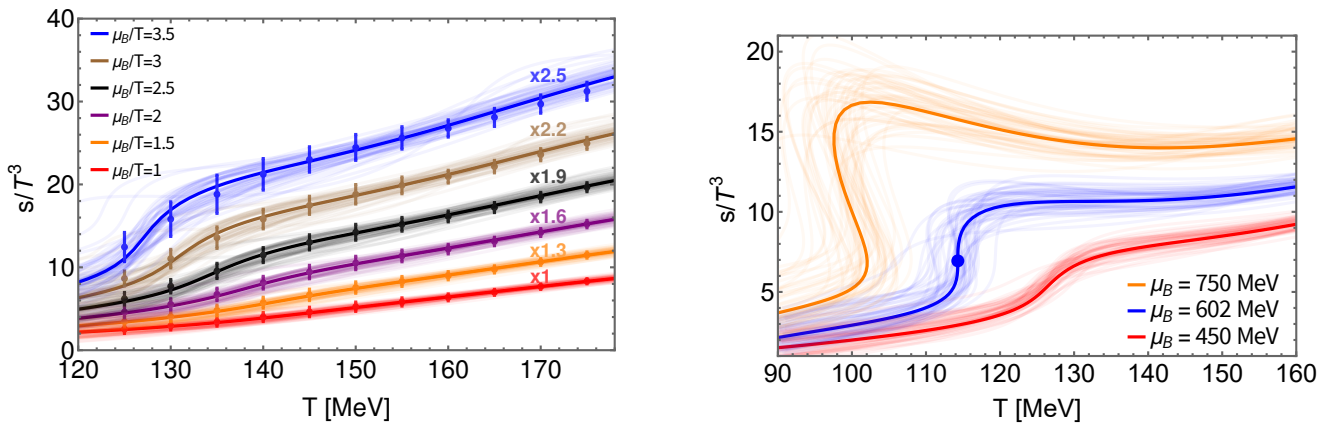


FIG. 2: Left panel: Scaled entropy density as a function of the temperature for different slices of constant μ_B/T . The curves are multiplied by different factors to avoid plotting overlap. Right panel: Scaled entropy density as a function of the temperature for different slices of constant baryochemical potential, $\mu_B = 450$ MeV (red lines, crossover regime), $\mu_B = 602$ MeV (blue lines, critical regime), $\mu_B = 750$ MeV (orange lines, mixed phase regime). The blue circle shows the critical point. In both panels, the solid curves correspond to the mean parametrization of lattice QCD results, while the translucent curves reflect the error propagation of the lattice QCD input via Monte Carlo sampling.

The coexistence curve $T_{cc}(\mu_B)$ at $\mu_B > \mu_{B,c}$ can be determined by the Maxwell construction of equal areas for entropy density, namely

$$\int_{s_1(T_{cc})}^{s_2(T_{cc})} \{T_s[\mu_B; T_0(s)] - T_{cc}(\mu_B)\} ds = 0,$$

where $T_0(s)$ is the value of T_0 corresponding to a given value s of the entropy density, and $s_1(T_{cc})$ and $s_2(T_{cc})$ are the entropy densities in the two coexisting phases.

Utilizing the above equations and a parametrized lattice QCD input, we obtain $T_{0,c} = 140.9 \pm 2.0$ MeV, and

$$(T_c, \mu_{B,c}) = (114.3 \pm 6.9, 602.1 \pm 62.1) \text{ MeV} \quad (11)$$

for the CP location in the T - μ_B plane. The uncertainties are obtained using Gaussian error propagation of the lattice QCD input. The uncertainties in T_c and $\mu_{B,c}$ are (anti-)correlated, with a Pearson correlation coefficient of -0.91.

The obtained CP is shown in the T - μ_B plane in Fig. 3, together with the spinodals and the coexistence line. The shown covariance ellipse corresponds to the 68% confidence interval. We also cross-check the error estimate by sampling the (Gaussian) log-likelihood of our lattice QCD input parametrization and depicting the resulting spread of critical points by hazy gray circles in Fig. 3.

The obtained CP location is consistent with the possible continuation of the chiral crossover line [2], shown in Fig. 3 by the yellow band at $\mu_B < 400$ MeV. In the context of heavy-ion collisions, the CP should lie above the chemical freeze-out line where the hadron resonance gas model description of hadron yields applies. The chemical freeze-out bound on the lowest CP temperature obtained in Ref. [38] under $\mu_Q = \mu_S = 0$ conditions appropriate for our analysis is shown in Fig. 3 by the orange line,

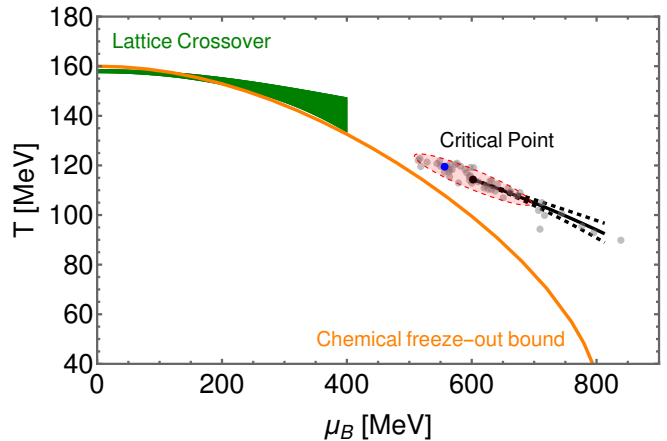


FIG. 3: The solid black point depicts the location of the QCD critical point extracted using the contours of constant entropy density based on lattice QCD data. The dashed ellipse corresponds to the 68% confidence interval and reflects the error propagation of the lattice input. The hazed gray points show the scatter of the critical points obtained by sampling the lattice QCD input within the lattice errors. The solid and dashed black lines depict the coexistence curve and the spinodals, respectively. The blue point shows the mean location of the QCD critical point obtained using smoothing splines instead of parametrization. The yellow band shows the chiral crossover line from [2]. The orange line corresponds to the heavy-ion chemical freeze-out bound on the CP from [38].

and it lies ~ 10 MeV below our CP estimate in temperature. Based on the μ_B dependence of the chemical freeze-out curve [39], we find that the collision energy range of $\sqrt{s_{NN}} = 4 \div 6$ GeV is in the closest vicinity to our CP location estimate.

Our results are generally compatible with other CP estimates in recent literature based on different approaches,

such as the Dyson-Schwinger equation, functional renormalization group, or holography [9–12]. Estimates based on the analysis of Yang-Lee edge singularities seem to yield somewhat smaller T or μ_B values [13, 14], although these analyses are based on high-order baryon susceptibilities for which no continuum-extrapolated data are available yet, and currently have large systematic uncertainties and cut-off effects. Our value of T_c is considerably lower, however, than suggested by a recent finite-size scaling analysis of proton cumulants in heavy-ion collisions [26].

Consistency checks. Lattice QCD groups typically use splines to perform analyses on higher order fluctuations [5, 40], rather than parameterizations. We performed a corresponding check by using a smoothed spline interpolation of the lattice data for $s(T)$ and $\chi_2^B(T)$ to calculate $\alpha_2(T)$ and determine the CP (see the Supplemental Material). The resulting CP is found at $(T_c, \mu_{B,c}) = (119.5 \pm 5.4, 556.5 \pm 49.8)$ MeV. The mean value is inside the 68% confidence ellipse obtained with the parametrization, as shown by the blue point in Fig. 3.

As a different check, we utilized the parameterization of the $\mu_B = 0$ equation of state from the HotQCD Collaboration from Ref. [34] in place of our Eq. (7) for the entropy density. Using the mean values of the parameters, we obtain a CP located at $(T_c, \mu_{B,c}) = (111.4, 634.8)$ MeV which is, again, well inside our 68% confidence region.

We also checked the performance of our method against a couple of solvable models. The holographic model [35] constrained by lattice QCD data contains a CP at $(T_c, \mu_{B,c}) \simeq (103, 599)$ MeV [12]. When we use the input for $s(T_0)$ and $\chi_2^B(T_0)$ to determine $\alpha_2(T_0)$ in the same holographic model, we obtain a CP at $(T_c, \mu_{B,c}) \simeq (104.5, 637.6)$ MeV using our new expansion method. This estimate is consistent with the true CP location within a relative error of 1.4% and 6.4% in T and μ_B , respectively.

Another useful test is provided by the ideal HRG model, which has no CP. Thus, this model can be used to test whether our method may produce a fake signature of a CP. Utilizing an open source HRG code [41], we tested that the CP equation $\alpha_2''(T_{0,c}) = 0$ [Eq. (10)] is not satisfied at any $T_0 < 200$ MeV in the ideal HRG model, as expected for a model not containing a CP.

Roberge-Weiss endpoint. The equation (6) determining the value of T_0 corresponding to a CP permits a second solution at $\tilde{T}_{0,c} = 160.2 \pm 1.8$ MeV. The value of $\alpha_2'(\tilde{T}_{0,c})$ at this temperature is positive and, therefore, the critical chemical potential $\tilde{\mu}_{B,c}$ given by Eq. (9) is purely imaginary. By calculating the critical temperature through Eq. (8) we obtain

$$\tilde{T}_c = 197.1 \pm 7.1 \text{ MeV}, \quad \frac{\tilde{\mu}_{B,c}}{\tilde{T}_c} = i(3.50 \pm 0.30). \quad (12)$$

Remarkably, this value is close to where the Roberge-Weiss (RW) transition endpoint [42–44] is expected in

the plane of temperature and imaginary chemical potential, namely $T_{RW} = 208 \pm 5$ MeV [45, 46], and $\mu_{B,RW}/T_{RW} = i\pi$ [42]. One should note that our new expansion does not explicitly incorporate the RW periodicity $\mu_B \rightarrow \mu_B + i2\pi T$ of the partition function and the exact relation between the extracted CP at imaginary μ_B and the RW endpoint requires further investigations.

Conclusion. In this Letter, a novel method for determining the QCD critical point is proposed, based on the crossings of constant entropy density contours. The expansion (3) of the $s = \text{const.}$ line away from $\mu_B = 0$ is utilized, which overcomes the shortcomings of other expansion schemes by permitting the description of a CP and a first-order phase transition already at the leading expansion order. Utilizing this novel expansion and the continuum-extrapolated lattice QCD data from the Wuppertal-Budapest collaboration for entropy density $s(T)$ and baryon susceptibility $\chi_2^B(T)$ as input, we find evidence for the presence of the QCD critical point in the QCD phase diagram at $(T_c, \mu_{B,c}) = (114.3 \pm 6.9, 602.1 \pm 62.1)$ MeV, with the quoted uncertainty corresponding exclusively to the propagation of lattice QCD errors for $s(T)$ and $\chi_2^B(T)$.

The analysis can be improved in the future by utilizing more precise lattice input. The CP is determined by the behavior of the coefficient α_2 and its temperature derivatives, which are expressed in terms of entropy density and baryon susceptibility. Therefore, a more direct determination of α_2 and its temperature derivatives on the lattice can significantly improve the statistical error. An analysis of the truncation error due to using the expansion (3) at order $\mathcal{O}(\mu_B^2)$ is also important. Such an analysis will require the accurate determination of higher-order susceptibilities such as χ_4^B , and high-order temperature derivatives. Alternatively, one could also utilize direct extrapolations of entropy density contours from zero and imaginary μ_B toward positive, real μ_B , and analyze the possible emergence of their crossings. Given that the extracted values of $T_{0,c}$ are of order $T_{0,c} \simeq 140$ MeV, and the analysis relies on temperature derivatives, it is suggestive of expanding the corresponding lattice QCD simulations to lower temperatures, possibly down to $T \sim 120$ MeV.

Acknowledgements. J.N. and M.H. thank Abhishek Kodumagulla for collaboration in the earliest stages of this work. V.V. acknowledges fruitful discussions with Volker Koch. This material is based upon work supported by the National Science Foundation under grants No. PHY-2208724, and PHY-2116686, and within the framework of the MUSES collaboration, under grant number No. OAC- 2103680. This material is also based upon work supported by the U.S. Department of Energy, Office of Science, Office of Nuclear Physics, under Award Number DE-SC0022023 and by the National Aeronautics and Space Agency (NASA) under Award Number 80NSSC24K0767. M.H. was supported in part by Universidade Estadual do Rio de Janeiro, within the Programa de Apoio à Docência (PAPD). J.N. is partly

supported by the U.S. Department of Energy, Office of

Science, Office for Nuclear Physics under Award No. DE-SC0023861.

-
- [1] Y. Aoki, Z. Fodor, S. D. Katz, and K. K. Szabo, The QCD transition temperature: Results with physical masses in the continuum limit, *Phys. Lett. B* **643**, 46 (2006), arXiv:hep-lat/0609068.
- [2] S. Borsanyi, Z. Fodor, J. N. Guenther, R. Kara, S. D. Katz, P. Parotto, A. Pasztor, C. Ratti, and K. K. Szabo, QCD Crossover at Finite Chemical Potential from Lattice Simulations, *Phys. Rev. Lett.* **125**, 052001 (2020), arXiv:2002.02821 [hep-lat].
- [3] A. Bazavov *et al.* (HotQCD), Chiral crossover in QCD at zero and non-zero chemical potentials, *Phys. Lett. B* **795**, 15 (2019), arXiv:1812.08235 [hep-lat].
- [4] V. Vovchenko, J. Steinheimer, O. Philipsen, and H. Stoecker, Cluster Expansion Model for QCD Baryon Number Fluctuations: No Phase Transition at $\mu_B/T < \pi$, *Phys. Rev. D* **97**, 114030 (2018), arXiv:1711.01261 [hep-ph].
- [5] D. Bollweg, J. Goswami, O. Kaczmarek, F. Karsch, S. Mukherjee, P. Petreczky, C. Schmidt, and P. Scior (HotQCD), Taylor expansions and Padé approximants for cumulants of conserved charge fluctuations at nonvanishing chemical potentials, *Phys. Rev. D* **105**, 074511 (2022), arXiv:2202.09184 [hep-lat].
- [6] S. Borsanyi, Z. Fodor, J. N. Guenther, P. Parotto, A. Pasztor, L. Pirelli, K. K. Szabo, and C. H. Wong, QCD deconfinement transition line up to $\mu_B = 400$ MeV from finite volume lattice simulations, (2024), arXiv:2410.06216 [hep-lat].
- [7] A. Bzdak, S. Esumi, V. Koch, J. Liao, M. Stephanov, and N. Xu, Mapping the Phases of Quantum Chromodynamics with Beam Energy Scan, *Phys. Rept.* **853**, 1 (2020), arXiv:1906.00936 [nucl-th].
- [8] L. Du, A. Sorensen, and M. Stephanov, The QCD phase diagram and Beam Energy Scan physics: a theory overview (2024) arXiv:2402.10183 [nucl-th].
- [9] W.-j. Fu, J. M. Pawłowski, and F. Rennecke, QCD phase structure at finite temperature and density, *Phys. Rev. D* **101**, 054032 (2020), arXiv:1909.02991 [hep-ph].
- [10] P. J. Gunkel and C. S. Fischer, Locating the critical endpoint of QCD: Mesonic backcoupling effects, *Phys. Rev. D* **104**, 054022 (2021), arXiv:2106.08356 [hep-ph].
- [11] F. Gao and J. M. Pawłowski, Chiral phase structure and critical end point in QCD, *Phys. Lett. B* **820**, 136584 (2021), arXiv:2010.13705 [hep-ph].
- [12] M. Hippert, J. Grefa, T. A. Manning, J. Noronha, J. Noronha-Hostler, I. Portillo Vazquez, C. Ratti, R. Rougemont, and M. Trujillo, Bayesian location of the QCD critical point from a holographic perspective, (2023), arXiv:2309.00579 [nucl-th].
- [13] G. Basar, QCD critical point, Lee-Yang edge singularities, and Padé resummations, *Phys. Rev. C* **110**, 015203 (2024), arXiv:2312.06952 [hep-th].
- [14] D. A. Clarke, P. Dimopoulos, F. Di Renzo, J. Goswami, C. Schmidt, S. Singh, and K. Zambello, Searching for the QCD critical endpoint using multi-point Padé approximations, (2024), arXiv:2405.10196 [hep-lat].
- [15] M. A. Stephanov, K. Rajagopal, and E. V. Shuryak, Event-by-event fluctuations in heavy ion collisions and the QCD critical point, *Phys. Rev. D* **60**, 114028 (1999), arXiv:hep-ph/9903292.
- [16] Y. Hatta and M. A. Stephanov, Proton number fluctuation as a signal of the QCD critical endpoint, *Phys. Rev. Lett.* **91**, 102003 (2003), [Erratum: *Phys.Rev.Lett.* **91**, 129901 (2003)], arXiv:hep-ph/0302002.
- [17] M. A. Stephanov, Non-Gaussian fluctuations near the QCD critical point, *Phys. Rev. Lett.* **102**, 032301 (2009), arXiv:0809.3450 [hep-ph].
- [18] X. Luo and N. Xu, Search for the QCD Critical Point with Fluctuations of Conserved Quantities in Relativistic Heavy-Ion Collisions at RHIC : An Overview, *Nucl. Sci. Tech.* **28**, 112 (2017), arXiv:1701.02105 [nucl-ex].
- [19] J. Adam *et al.* (STAR), Nonmonotonic Energy Dependence of Net-Proton Number Fluctuations, *Phys. Rev. Lett.* **126**, 092301 (2021), arXiv:2001.02852 [nucl-ex].
- [20] M. Abdallah *et al.* (STAR), Cumulants and correlation functions of net-proton, proton, and antiproton multiplicity distributions in Au+Au collisions at energies available at the BNL Relativistic Heavy Ion Collider, *Phys. Rev. C* **104**, 024902 (2021), arXiv:2101.12413 [nucl-ex].
- [21] A. Pandav [for STAR collaboration], (2024), talk at CPOD 2024 conference (20-24 May 2024, Berkeley, CA, USA).
- [22] P. Braun-Munzinger, B. Friman, K. Redlich, A. Rustamov, and J. Stachel, Relativistic nuclear collisions: Establishing a non-critical baseline for fluctuation measurements, *Nucl. Phys. A* **1008**, 122141 (2021), arXiv:2007.02463 [nucl-th].
- [23] V. Vovchenko, V. Koch, and C. Shen, Proton number cumulants and correlation functions in Au-Au collisions at $s_{NN}=7.7-200$ GeV from hydrodynamics, *Phys. Rev. C* **105**, 014904 (2022), arXiv:2107.00163 [hep-ph].
- [24] E. S. Fraga, L. F. Palhares, and P. Sorensen, Finite-size scaling as a tool in the search for the QCD critical point in heavy ion data, *Phys. Rev. C* **84**, 011903 (2011), arXiv:1104.3755 [hep-ph].
- [25] R. A. Lacey, Indications for a Critical End Point in the Phase Diagram for Hot and Dense Nuclear Matter, *Phys. Rev. Lett.* **114**, 142301 (2015), arXiv:1411.7931 [nucl-ex].
- [26] A. Sorensen and P. Sorensen, Locating the critical point for the hadron to quark-gluon plasma phase transition from finite-size scaling of proton cumulants in heavy-ion collisions, (2024), arXiv:2405.10278 [nucl-th].
- [27] C. R. Allton, S. Ejiri, S. J. Hands, O. Kaczmarek, F. Karsch, E. Laermann, and C. Schmidt, The Equation of state for two flavor QCD at nonzero chemical potential, *Phys. Rev. D* **68**, 014507 (2003), arXiv:hep-lat/0305007.
- [28] C. R. Allton, M. Doring, S. Ejiri, S. J. Hands, O. Kaczmarek, F. Karsch, E. Laermann, and K. Redlich, Thermodynamics of two flavor QCD to sixth order in quark chemical potential, *Phys. Rev. D* **71**, 054508 (2005), arXiv:hep-lat/0501030.
- [29] S. Borsanyi, G. Endrodi, Z. Fodor, S. D. Katz, S. Krieg, C. Ratti, and K. K. Szabo, QCD equation of state

- at nonzero chemical potential: continuum results with physical quark masses at order mu^2 , JHEP **08**, 053, arXiv:1204.6710 [hep-lat].
- [30] A. Bazavov *et al.*, The QCD Equation of State to $\mathcal{O}(\mu_B^6)$ from Lattice QCD, Phys. Rev. D **95**, 054504 (2017), arXiv:1701.04325 [hep-lat].
- [31] D. Bollweg, D. A. Clarke, J. Goswami, O. Kaczmarek, F. Karsch, S. Mukherjee, P. Petreczky, C. Schmidt, and S. Sharma (HotQCD), Equation of state and speed of sound of (2+1)-flavor QCD in strangeness-neutral matter at nonvanishing net baryon-number density, Phys. Rev. D **108**, 014510 (2023), arXiv:2212.09043 [hep-lat].
- [32] R. V. Gavai and S. Gupta, The Critical end point of QCD, Phys. Rev. D **71**, 114014 (2005), arXiv:hep-lat/0412035.
- [33] S. Borsányi, Z. Fodor, J. N. Guenther, R. Kara, S. D. Katz, P. Parotto, A. Pásztor, C. Ratti, and K. K. Szabó, Lattice QCD equation of state at finite chemical potential from an alternative expansion scheme, Phys. Rev. Lett. **126**, 232001 (2021), arXiv:2102.06660 [hep-lat].
- [34] A. Bazavov *et al.* (HotQCD), Equation of state in (2+1)-flavor QCD, Phys. Rev. D **90**, 094503 (2014), arXiv:1407.6387 [hep-lat].
- [35] R. Critelli, J. Noronha, J. Noronha-Hostler, I. Portillo, C. Ratti, and R. Rougemont, Critical point in the phase diagram of primordial quark-gluon matter from black hole physics, Phys. Rev. D **96**, 096026 (2017), arXiv:1706.00455 [nucl-th].
- [36] S. Borsanyi, Z. Fodor, C. Hoelbling, S. D. Katz, S. Krieg, and K. K. Szabo, Full result for the QCD equation of state with 2+1 flavors, Phys. Lett. B **730**, 99 (2014), arXiv:1309.5258 [hep-lat].
- [37] M. Kahangirwe, S. A. Bass, E. Bratkovskaya, J. Jahan, P. Moreau, P. Parotto, D. Price, C. Ratti, O. Soloveva, and M. Stephanov, Finite density QCD equation of state: Critical point and lattice-based T' expansion, Phys. Rev. D **109**, 094046 (2024), arXiv:2402.08636 [nucl-th].
- [38] A. Lysenko, M. I. Gorenstein, R. Poberezhniuk, and V. Vovchenko, Chemical freeze-out curve in heavy-ion collisions and the QCD critical point, (2024), arXiv:2408.06473 [nucl-th].
- [39] V. Vovchenko, V. V. Begun, and M. I. Gorenstein, Hadron multiplicities and chemical freeze-out conditions in proton-proton and nucleus-nucleus collisions, Phys. Rev. C **93**, 064906 (2016), arXiv:1512.08025 [nucl-th].
- [40] S. Borsanyi, Z. Fodor, J. N. Guenther, S. D. Katz, P. Parotto, A. Pásztor, D. Pesznyak, K. K. Szabo, and C. H. Wong, Continuum-extrapolated high-order baryon fluctuations, Phys. Rev. D **110**, L011501 (2024), arXiv:2312.07528 [hep-lat].
- [41] V. Vovchenko and H. Stoecker, Thermal-FIST: A package for heavy-ion collisions and hadronic equation of state, Comput. Phys. Commun. **244**, 295 (2019), arXiv:1901.05249 [nucl-th].
- [42] A. Roberge and N. Weiss, Gauge Theories With Imaginary Chemical Potential and the Phases of QCD, Nucl. Phys. B **275**, 734 (1986).
- [43] O. Philipsen and C. Pinke, Nature of the Roberge-Weiss transition in $N_f = 2$ QCD with Wilson fermions, Phys. Rev. D **89**, 094504 (2014), arXiv:1402.0838 [hep-lat].
- [44] C. Czaban, F. Cuteri, O. Philipsen, C. Pinke, and A. Sciarra, Roberge-Weiss transition in $N_f = 2$ QCD with Wilson fermions and $N_\tau = 6$, Phys. Rev. D **93**, 054507 (2016), arXiv:1512.07180 [hep-lat].
- [45] C. Bonati, M. D'Elia, M. Mariti, M. Mesiti, F. Negro, and F. Sanfilippo, Roberge-Weiss endpoint at the physical point of $N_f = 2 + 1$ QCD, Phys. Rev. D **93**, 074504 (2016), arXiv:1602.01426 [hep-lat].
- [46] P. Dimopoulos, L. Dini, F. Di Renzo, J. Goswami, G. Nicotra, C. Schmidt, S. Singh, K. Zambello, and F. Ziesché, Contribution to understanding the phase structure of strong interaction matter: Lee-Yang edge singularities from lattice QCD, Phys. Rev. D **105**, 034513 (2022), arXiv:2110.15933 [hep-lat].
- [47] C. De Boor, *A Practical Guide to Splines*, Applied Mathematical Sciences (Springer New York, 1978).

SUPPLEMENTAL MATERIAL

Expansion coefficients

The coefficients α_{2n} of the constant entropy density expansion

$$T_s(\mu_B; T_0) \approx T_0 + \sum_{n=1}^N \alpha_{2n}(T_0) \frac{\mu_B^{2n}}{(2n)!} + \mathcal{O}(\mu_B^{2(N+1)}), \quad (\text{A.1})$$

correspond to the derivatives of the temperature T with respect to μ_B while holding the entropy density s fixed,

$$\alpha_{2n}(T_0) = \left(\frac{\partial^{2n} T}{\partial \mu_B^{2n}} \right) \Big|_{s, T=T_0, \mu_B=0}. \quad (\text{A.2})$$

To evaluate these derivatives, we write the entropy density differential ds

$$ds = (\partial s / \partial T)_{\mu_B} dT + (\partial s / \partial \mu_B)_T d\mu_B, \quad (\text{A.3})$$

or

$$dT = \frac{1}{(\partial s / \partial T)_{\mu_B}} ds - \frac{(\partial s / \partial \mu_B)_T}{(\partial s / \partial T)_{\mu_B}} d\mu_B, \quad (\text{A.4})$$

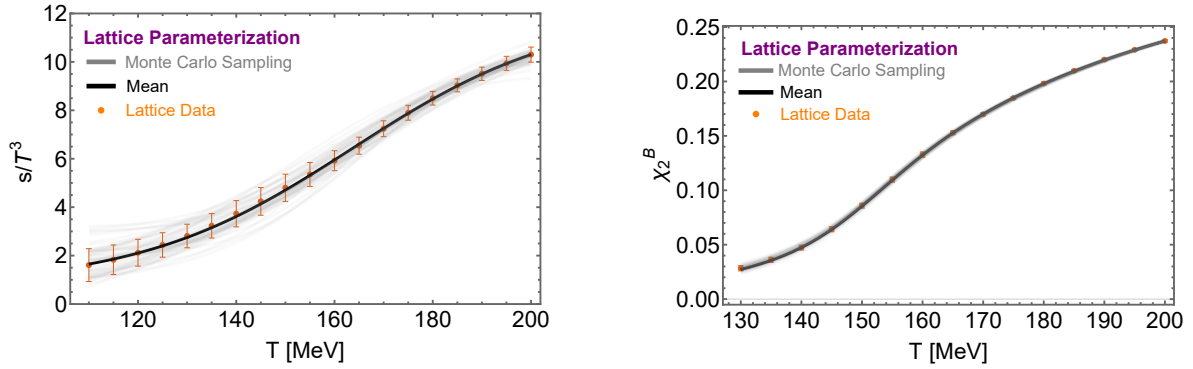


FIG. A.1: Scaled entropy density s/T^3 (left panel) and second order baryon number susceptibility χ_2^B (right panel) as functions of the temperature at $\mu_B = 0$. The orange symbols with error bars depict the lattice QCD data of the Wuppertal-Budapest collaboration [33, 36]. The solid black line corresponds to the parameterization of the lattice data using the mean parameter values, while the hazed black lines correspond to different Monte Carlo samples of the parameters reflecting the uncertainties in the lattice data.

thus

$$\left(\frac{\partial T}{\partial \mu_B}\right)_s = -\frac{(\partial s/\partial \mu_B)_T}{(\partial s/\partial T)_{\mu_B}} = -\frac{(\partial \rho_B/\partial T)_{\mu_B}}{(\partial s/\partial T)_{\mu_B}} = -\frac{\rho'_B}{s'}. \quad (\text{A.5})$$

This expression determines the change of the temperature with respect to μ_B along a contour of constant entropy density. Given that $\rho_B = 0$ for all temperatures at $\mu_B = 0$, this derivative vanishes at $\mu_B = 0$:

$$\alpha_1(T_0) = \left(\frac{\partial T}{\partial \mu_B}\right)_s \Big|_{T=T_0, \mu_B=0} = 0. \quad (\text{A.6})$$

The coefficient α_2 reads

$$\alpha_2(T_0) = \left(\frac{\partial^2 T}{\partial \mu_B^2}\right)_s \Big|_{T=T_0, \mu_B=0}. \quad (\text{A.7})$$

We apply a derivative $(\partial/\partial \mu_B)_s$ to Eq. (A.5) and evaluate it using the chain rule, yielding

$$\begin{aligned} \left(\frac{\partial^2 T}{\partial \mu_B^2}\right)_s &= \left[\frac{\partial(\partial T/\partial \mu_B)_s}{\partial \mu_B}\right]_T + \left[\frac{\partial(\partial T/\partial \mu_B)_s}{\partial T}\right]_{\mu_B} \left(\frac{\partial T}{\partial \mu_B}\right)_s \\ &= -\frac{2T\chi_2^B + T^2\chi_2^{B'}}{s'} + \frac{\rho'_B \rho''_B}{[s']^2} + \left[\frac{\rho'_B s''}{(s')^2} - \frac{\rho''_B}{s'}\right] \left(\frac{\partial T}{\partial \mu_B}\right)_s, \end{aligned} \quad (\text{A.8})$$

where we took into account that $\rho_B = T^3\chi_1^B$ and $(\partial\chi_1^B/\partial\mu_B)_T = \chi_2^B/T$. At $\mu_B = 0$, only the first term is non-zero, giving

$$\alpha_2(T_0) = \left(\frac{\partial^2 T}{\partial \mu_B^2}\right)_s \Big|_{T=T_0, \mu_B=0} = -\frac{2T_0\chi_2^B(T_0) + T_0^2\chi_2^{B'}(T_0)}{s'(T_0)}. \quad (\text{A.9})$$

Lattice QCD input and its description

Our method requires entropy density $s(T)$ and baryon number susceptibility $\chi_2^B(T)$ at vanishing chemical potential $\mu_B = 0$ as input. We utilize continuum-extrapolated lattice data for $s(T)$ and $\chi_2^B(T)$ of the Wuppertal-Budapest collaboration from Refs. [36] and [33], respectively. These lattice QCD data are shown in Fig. A.1.

Entropy density. As our method requires the use of temperature derivatives, we parametrize the lattice QCD input and its uncertainties. For the entropy density, we use the following function

$$\frac{s}{T^3} = a \cdot \tanh\left(\frac{T - T_0}{d}\right) + b. \quad (\text{A.10})$$

To determine the values of the parameters and their uncertainties, we perform a fit of the lattice data at temperatures $110 < T < 200$ MeV through χ^2 minimization. The expression for χ_s^2 (the index s indicates that it is the χ^2 for the entropy) reads

$$\chi_s^2 = \sum_{i,j=1}^N [(s/T^3)_i^{\text{param}} - (s/T^3)_i^{\text{lattice}}](\Sigma_s^{-1})_{ij}^{\text{lattice}} [(s/T^3)_j^{\text{param}} - (s/T^3)_j^{\text{lattice}}]. \quad (\text{A.11})$$

Here the sums runs over all lattice data points, where $i = 1$ corresponds to the lowest temperature, $T_1 = 110$ MeV and $i = N$ to the highest temperature, $T_N = 200$ MeV, used in the fit. All temperature points are equally spaced, with a step of $\Delta T = 5$ MeV. Σ_s is the covariance matrix describing the lattice errors and correlations among them. It is taken in the form

$$(\Sigma_s)_{ij}^{\text{lattice}} = (\sigma_s)_i (\sigma_s)_j \Gamma_s^{|i-j|}. \quad (\text{A.12})$$

Here $0 < \Gamma_s < 1$ is the covariance coefficient correlating the uncertainties between lattice data points at different temperatures. This choice was considered in Ref. [12] and implies stronger correlations between data points that are closer in temperatures. It was also indicated in Ref. [12] that a value of $\Gamma_s = 0.84$ describes the lattice data the best, and we use this value in the present analysis.

Parameter	Value	Covariance	a	b	T_0	d
a	5.65608	a	1.24081	-0.133316	-1.5958	13.4657
b	6.43026	b	-0.133316	0.232124	2.08816	-0.507437
T_0	163.681	T_0	-1.5958	2.08816	24.4358	-14.2532
d	43.3516	d	13.4657	-0.507437	-14.2532	161.338

TABLE I: Mean values of parameters describing the lattice QCD data on s/T^3 via parametrization (A.10) (left table) and their covariance matrix (right table). The units for T_0 are MeV.

Table I depicts the mean parameter values and the resulting covariance matrix obtained from fitting the lattice QCD data through χ_s^2 minimization. The left panel of Fig. A.1 shows the comparison of the resulting parametrization with lattice QCD data. The solid black line corresponds to the mean parameter values, showing excellent agreement with the mean values of the lattice data. The 50 hazy gray lines depict the results of the parametrization by sampling the parameter sets from a multi-Gaussian distribution with the mean vector and covariance matrix listed in Table I. The resulting spread of the lines accurately reflects the uncertainties in the lattice data.

Baryon number susceptibility. We parametrize the baryon number susceptibility $\chi_2^B(T)$ at $\mu_B = 0$ in the following form

$$\chi_2^B(T) = d_0 \left(\frac{2 \cdot m_p}{\pi \cdot x}\right)^{\frac{3}{2}} \cdot \frac{\exp\left(-\frac{m_p}{x}\right)}{1 + \left(\frac{x}{d_1}\right)^{d_2}} + d_3 \cdot \frac{\exp\left(-\frac{d_4^4}{x^4}\right)}{1 + \left(\frac{x}{d_1}\right)^{-d_2}}. \quad (\text{A.13})$$

Here $x = T/(200 \text{ MeV})$ and $m_p = (938/200) \approx 4.7$ is the mass of the proton mass in units of 200 MeV. This is a modified version of the parametrization used in Ref. [37], where we introduced an additional parameter d_0 and removed the parameter d_4 by setting it to zero. This modification leads to a more accurate description of the lattice data [33] on χ_2^B and its temperature derivative at $T \lesssim 145$ MeV. As in the case of entropy density, the determination of parameters and their covariance matrix proceeds by minimizing $\chi_{\chi_2^B}^2$:

$$\chi_{\chi_2^B}^2 = \sum_{i,j=1}^N [(\chi_2^B)_i^{\text{param}} - (\chi_2^B)_i^{\text{lattice}}](\Sigma_{\chi_2^B}^{-1})_{ij}^{\text{lattice}} [(\chi_2^B)_j^{\text{param}} - (\chi_2^B)_j^{\text{lattice}}], \quad (\text{A.14})$$

where the covariance matrix of the lattice uncertainties reads

$$(\Sigma_{\chi_2^B})_{ij}^{\text{lattice}} = (\sigma_{\chi_2^B})_i (\sigma_{\chi_2^B})_j \Gamma_{\chi_2^B}^{|i-j|}, \quad (\text{A.15})$$

Parameter	Value	Covariance	d_0	d_1	d_2	d_3	d_5
d_0	3.60763	d_0	0.136045	0.00112188	0.630763	0.000696749	0.00126876
d_1	0.750215	d_1	0.00112188	0.0000375329	0.00251407	$-6.53388 \cdot 10^{-6}$	-0.0000106728
d_2	21.1553	d_2	0.630763	0.00251407	7.31758	0.00923282	0.0167017
d_3	0.330518	d_3	0.000696749	$-6.53388 \cdot 10^{-6}$	0.00923282	0.0000223041	0.0000379904
d_5	0.758584	d_5	0.00126876	-0.0000106728	0.0167017	0.0000379904	0.0000664791

TABLE II: Mean values of parameters describing the lattice QCD data on χ_2^B via parametrization (A.13) (left table) and their covariance matrix (right table).

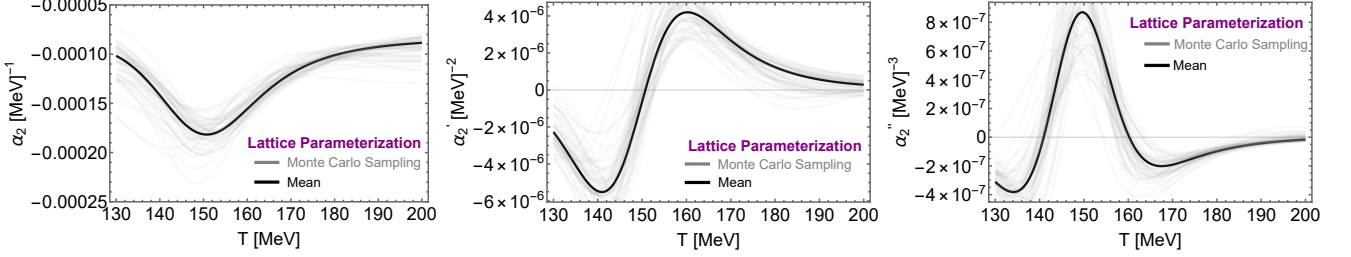


FIG. A.2: Temperature dependence of the second order expansion coefficient α_2 (left panel), and its first (middle panel) and second (right panel) temperature derivatives obtained using the parametrization of the lattice data. The black lines correspond to mean parameter values while hazy gray lines correspond to the Monte Carlo sampling of parameter values.

with the correlation coefficient $\Gamma_{\chi_2} = 0.84$ [12]. In contrast to the entropy density data, the lattice data for χ_2^B start at $T_1 = 130$ MeV in steps of $\Delta T = 5$ MeV. We use the lattice data in a range $130 \leq T \leq 200$ MeV in the fitting procedure. The resulting mean values of the parameters and their covariance matrix are listed in Table II.

The right panel of Fig. A.1 shows the comparison of our parametrization with the lattice data. As in the case of s/T^3 , the comparison indicates that our parametrization captures the behavior of both the means and the lattice errors accurately.

Expansion coefficient α_2 . Figure A.2 shows the temperature dependence of the expansion coefficient α_2 and its first and second derivatives, as obtained through Eq. (A.9) and using parameterizations (A.10) and (A.13) for s/T^3 and χ_2^B , respectively. As in Fig. A.1, the solid black curve corresponds to the mean parameter values, while the hazy gray curves correspond to Monte Carlo sampling of the parameters and reflect the propagation of the lattice data uncertainties.

Smoothing splines

One might question how our results depend on the particular parametrization we choose for the entropy and the second baryon susceptibility. To address this concern, we have also carried out a more agnostic analysis, using splines to interpolate the lattice results and Monte Carlo to propagate uncertainties. This analysis is discussed below.

For the error propagation, we create random pseudo-data such that its average reproduces the lattice results and its statistical errors reproduce the corresponding uncertainties. For each value of the temperature, T_i , with $i = 1, \dots, N$, we take

$$q_i = (q)_i^{\text{lattice}} + (\xi_q)_i \quad (\text{A.16})$$

where $q = s/T^3, \chi_2^B$. The statistical noise $(\xi_q)_i$ is randomly sampled from a Gaussian, of average $\langle (\xi_q)_i \rangle = 0$ and covariance

$$\langle (\xi_q)_i (\xi_{q'})_j \rangle = \delta_{qq'} (\sigma_q)_i (\sigma_{q'})_j \Gamma_q^{|i-j|}, \quad (\text{A.17})$$

where $(\sigma_q)_i$ are the lattice QCD uncertainties and we take the correlation coefficient $\Gamma_q = 0.84$ [12]. For each quantity $q = s/T^3, \chi_2^B$, we sample a thousand pseudo-data realizations $\{q_i\}$.

We then model the random pseudo-data sample with splines, so we can perform differentiation in a well-controlled way. A naive interpolation with splines would go through each point in the random pseudo-data, leading to artifacts

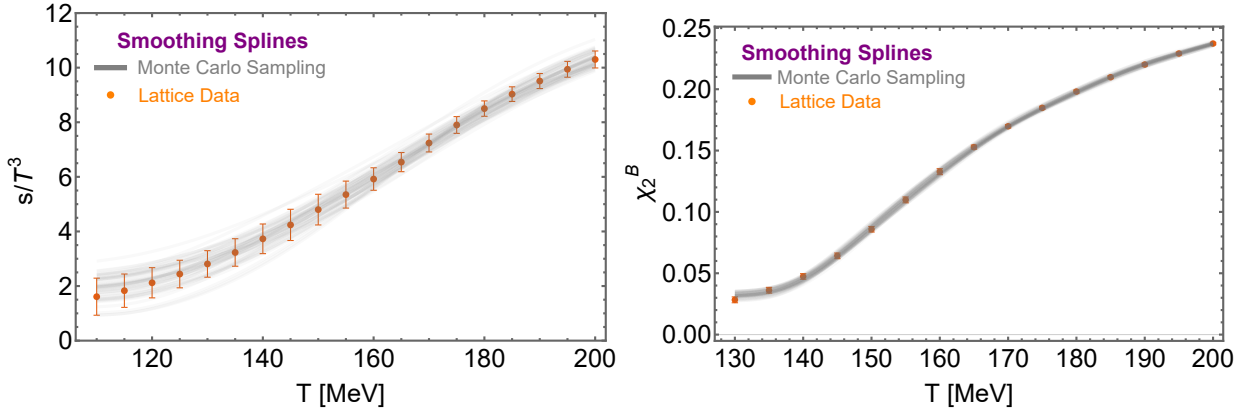


FIG. A.3: Same as Fig. A.1 but using smoothing splines for describing the lattice data instead of parametrization.

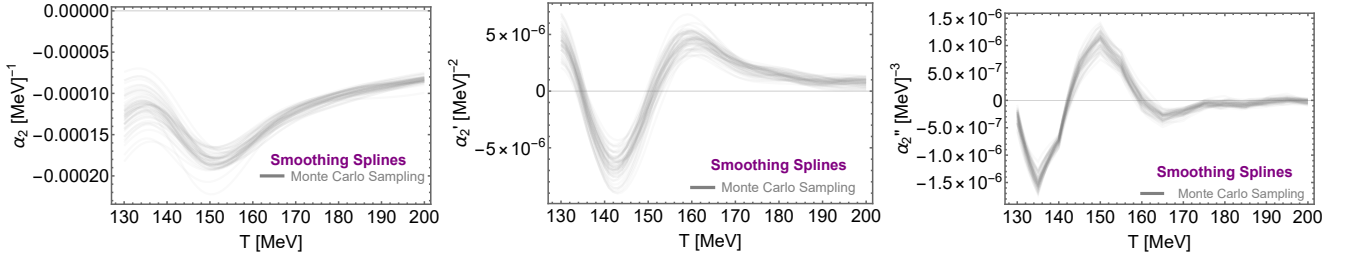


FIG. A.4: Same as Fig. A.2 but using smoothing splines for describing the lattice data instead of parametrization.

in the derivatives due to overfitting. Thus, we instead fit the pseudo-data with cubic smoothing splines [47]. We take natural cubic splines $f_q(T)$, with knots at the different T_i , constructed to minimize [47]

$$\tilde{\chi}_q[f_q]^2 = p_q \sum_{i=1}^N \left(\frac{q_i - f_q(T_i)}{(\sigma_q)_i} \right)^2 + (1 - p_q) \int_{T_1}^{T_N} dT (f_q''(T))^2, \quad (\text{A.18})$$

which favors smoother splines. Following [47], we pick the parameter p_q in Eq. (A.18) just large enough that

$$S[f_q] \equiv \sum_{i=1}^N \left(\frac{q_i - f_q(T_i)}{(\sigma_q)_i} \right)^2 \leq N. \quad (\text{A.19})$$

This procedure leads to an ensemble of functions that reproduce, to good accuracy, the lattice QCD results and uncertainties at $T = T_i$, $i = 1, \dots, N$, whilst displaying smooth, well-behaved derivatives. The smooth splines for entropy density and baryon number susceptibility are shown in Fig. A.3, where the smoothed splines performed on the pseudo data samples are in hazy gray lines compared to the lattice data. One can see good agreement with the lattice data and their errors, with the possible exception of the lowest temperature point for χ_2^B , which may be reflecting splining artefacts at the boundary.

From the splines obtained for each of the pseudo-data sets, we compute the coefficient $\alpha_2(T_0)$ and its temperature derivatives given in Fig. A.4. These show good agreement with the results obtained using the parametrization, again, with the possible exception of the lowest temperatures $T \lesssim 135$ MeV at the boundary. We use α_2 and its derivatives to determine the location of the CP, computing the mean and standard deviation of T_c and $\mu_{B,c}$ to obtain

$$(T_c, \mu_{B,c}) = (119.5 \pm 5.4, 556.5 \pm 49.8) \text{ MeV}, \quad (\text{A.20})$$

which agrees with our main result within one sigma. This can be seen in Fig. A.5, where the blue ellipse is the covariance ellipse at 68% confidence level and reflects the lattice QCD input's error propagation. To calculate this ellipse, a thousand samples were generated and splining was performed based on Eq. (A.18). The covariance ellipse is above the lowest temperature bound of the chemical freezeout curve described by the HRG input given in [38], while also being in agreement with the covariance ellipse (red) obtained using the parametrization shown in Fig. A.2.

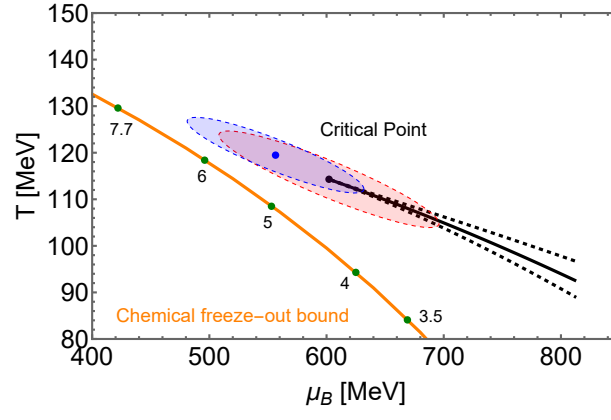


FIG. A.5: Same as Fig. 3 of the main text, but additionally showing the 68% confidence ellipse (blue ellipse) for the CP location obtained using smoothing splines. The green points show various chemical freeze-out points for different collision energies.